

## Research Article

# Thermo-Structural Behaviour Prediction of the Nose Cap of a Hypersonic Vehicle Based on Multifield Coupling

Xuewen Sun <sup>1,2</sup> Haibo Yang <sup>1,2,3</sup> and Tao Mi <sup>1,4</sup>

<sup>1</sup>School of Mechanical Engineering, University of Science and Technology Beijing, Beijing 100083, China

<sup>2</sup>Key Laboratory of Fluid Interaction with Material, Ministry of Education, Beijing 100083, China

<sup>3</sup>Centre of Excellence for Advanced Materials, Dongguan 523808, China

<sup>4</sup>School of Materials Engineering, North China Institute of Aerospace Engineering, Langfang 065000, China

Correspondence should be addressed to Haibo Yang; yhb@ustb.edu.cn

Received 24 July 2019; Revised 2 November 2019; Accepted 7 November 2019; Published 23 January 2020

Academic Editor: Timothy Lee

Copyright © 2020 Xuewen Sun et al. This is an open access article distributed under the Creative Commons Attribution License, which permits unrestricted use, distribution, and reproduction in any medium, provided the original work is properly cited.

The analysis of thermo-structural behaviour is crucial to the nose cap of a hypersonic vehicle under aerothermodynamic loads. Considering chemical nonequilibrium of the flow field, heat transfer, and deformation of the structure, a fluid-thermal-structural coupling model of the typical nose cap was established. The coupling relation between the flow field and nose cap was analyzed. The results show that the fluid-thermal-structural model can effectively predict the response of the nose cap under a hypersonic environment. The highest temperature and the peak of maximum principal stress appear at the front of the nose cap at an initial stage. As time goes on, the highest temperature increases gradually and the peak of maximum principal stress decreases after reaching a certain value. The position of the peak of maximum principal stress gradually moves to the inside of the nose cap and eventually stabilizes. With the increase in the Mach number, the highest temperature and the peak of maximum principal stress of the nose cap increase. The fluid-thermal-structural coupling model can provide guidance for the optimal design of the nose cap of a hypersonic vehicle.

## 1. Introduction

The hypersonic flight within the atmosphere can result in severe aerodynamic heating phenomena, which poses a major challenge for the thermal protection design of hypersonic vehicles [1]. When a hypersonic vehicle returns back to the earth crossing the atmosphere at a speed of 7~8 km/s, the nose cap is subjected to the heat flux up to 10 MW/m<sup>2</sup>, or even higher, due to the combination of shock wave and viscous friction of the surrounding air [2]. In order to protect the aircraft from damage under aerothermodynamic loads, design of the nose cap is particularly important. Accurate response prediction is the basis of nose cap design [3, 4]. There is strong coupling among hypersonic flow field, heat transfer, and deformation of the nose cap. When the nose cap is subjected to the aerothermodynamic loads, high temperature of the structure will cause the change of material physical parameters and large temperature gradient will result in thermal stress and deformation. In addition, the

structural deformation will affect the heat flux and pressure distributions along the wall of the structure, thus forming a complex thermo-mechanical coupling issue [5, 6]. Therefore, it is necessary to establish a fluid-thermal-structural coupling model to predict the hypersonic flow field, transient temperature, and deformation of the nose cap.

The research of fluid-thermal-structural coupling is one of the key issues in the development of a hypersonic vehicle. Many efforts have been made to improve the understanding of the multiphysical coupling of a hypersonic vehicle. In References [7, 8], the coupling model of the nose cap and hypersonic flow was established, and the effect of an attack angle on the nose cap response was analyzed. The ablation was predicted by using the moving mesh algorithm. Chen et al. studied the model of the leading edge of the wing, analyzed the mechanism of the coupling process, and obtained the distribution of temperature and stress of the leading edge at different times [9, 10]. Munk et al. used the coupling model to optimize the wing, and the influence of the coupling model

on the optimization design of the wing was analyzed [11]. References [12, 13] studied the effect of fluid-thermal-structural coupling on the response of a flat plate. Bhide et al. established a three-dimensional coupling model of a rectangular nozzle which provided some references for the optimization and improvement of the nozzle [14]. Guo et al. took the spine blunt body of aircraft as the research object, established the fluid-thermal-structural coupling model, analyzed the thermal response of the model, and obtained that the blunt body with longer spike had better thermal protection performance [15]. In References [16, 17], different coupling calculation methods were proposed for the fluid-thermal-structural coupling issue, and the effects on the accuracy and efficiency of calculation were studied. Multiphysical coupling of a hypersonic vehicle is a complex issue. In most of the previous researches on the response of the nose cap, a one-way coupling method was adopted, ignoring the influence of structural response on aerothermodynamic loads, which will affect the accuracy of prediction results.

The present work focuses on the establishment of a two-way fluid-thermal-structural coupling model. In the model, chemical nonequilibrium of the flow field, heat transfer, and deformation of the structure are considered. The purpose is to gain an insight into thermal-structural features of the nose cap. The numerical results are expected to provide technical support to the nose cap design of a hypersonic vehicle.

## 2. Governing Equations and Coupling Strategy

*2.1. Governing Equations of Aerodynamic Flow.* For the compressible viscous chemical nonequilibrium flow, the Navier-Stokes equations with a chemical source term are expressed as follows:

$$\frac{\partial Q}{\partial t} + \frac{\partial E}{\partial x} + \frac{\partial F}{\partial y} - \left( \frac{\partial E_v}{\partial x} + \frac{\partial F_v}{\partial y} \right) = S,$$

$$Q = \begin{bmatrix} \rho_1 \\ \vdots \\ \rho_{ns} \\ \rho u \\ \rho v \\ \rho E \\ \rho e_{ve} \end{bmatrix},$$

$$E = \begin{bmatrix} \rho_1 u \\ \vdots \\ \rho_{ns} u \\ \rho u^2 + p \\ \rho uv \\ \rho Hu \\ \rho e_{ve} u \end{bmatrix},$$

$$F = \begin{bmatrix} \rho_1 v \\ \vdots \\ \rho_{ns} v \\ \rho uv \\ \rho v^2 + p \\ \rho Hv \\ \rho e_{ve} v \end{bmatrix},$$

$$S = \begin{bmatrix} \dot{\omega}_1 \\ \vdots \\ \dot{\omega}_{ns} \\ 0 \\ 0 \\ 0 \\ \dot{\omega}_{ve} \end{bmatrix},$$

$$E_v = \begin{bmatrix} q_{x1} \\ \vdots \\ q_{xns} \\ \tau_{xx} \\ \tau_{xy} \\ u\tau_{xx} + v\tau_{xy} + q_x + q_{vex} + \rho \sum_{i=1}^{ns} D_{im} h_i \frac{\partial Y_i}{\partial x} \\ q_{vex} + \rho \sum_{i=mol} D_{im} e_{ve}^i \frac{\partial Y_i}{\partial x} \end{bmatrix},$$

$$F_v = \begin{bmatrix} q_{y1} \\ \vdots \\ q_{yns} \\ \tau_{yx} \\ \tau_{yy} \\ u\tau_{yx} + v\tau_{yy} + q_y + q_{vey} + \rho \sum_{i=1}^{ns} D_{im} h_i \frac{\partial Y_i}{\partial y} \\ q_{vey} + \rho \sum_{i=mol} D_{im} e_{ve}^i \frac{\partial Y_i}{\partial y} \end{bmatrix},$$

(1)

where  $Q$  is the conservative variable and  $E$  and  $F$  are inviscid fluxes in  $x$  and  $y$  directions, respectively.  $E_v$  and  $F_v$  are viscous fluxes in  $x$  and  $y$  directions, respectively.  $S$  is the source term reflecting the effect of chemical nonequilibrium.  $u$  and  $v$  are the velocities in  $x$  and  $y$  directions, respectively.  $p$ ,  $\rho$ , and  $Y_i$  are the pressure, density, and mass fraction of each

component of the gas, respectively.  $q_{xi}$  and  $q_{yi}$  are the diffusivity of components in the  $x$  and  $y$  directions, respectively.  $D_{im}$  and  $h_i$  are the diffusion coefficient and the absolute enthalpy per unit mass of components, respectively.  $q_x$  and  $q_y$  and  $q_{vex}$  and  $q_{vey}$  are translational-rotational heat fluxes and vibrational heat fluxes in  $x$  and  $y$  directions, respectively.  $\dot{\omega}_i$  and  $\dot{\omega}_{ve}$  are the component  $i$  mass generation rate and vibration energy, respectively.

The Gupta chemical kinetic model is used to calculate the component change caused by chemical reactions which contain NS components and NR chemical reactions. The chemical reaction equation is as follows [18]:

$$\sum_{s=1}^{NS} \alpha_{r,s} Z_s \stackrel{k_{f,r}}{\rightleftharpoons} \sum_{s=1}^{NS} \beta_{r,s} Z_s \quad (r = 1, 2, \dots, NR), \quad (2)$$

where  $Z_s$  is the chemical component.  $\alpha_{r,s}$  and  $\beta_{r,s}$  are the stoichiometric coefficients of reactants and products, respectively.  $k_{f,r}$  and  $k_{b,r}$  are the positive reaction rate and reverse reaction rate, respectively, in which subscripts  $f$  and  $b$  represent the positive reaction and reverse reaction, respectively. The chemical reaction rates  $k_{f,r}$  and  $k_{b,r}$  are obtained by the Arrhenius formula.

$$\begin{cases} k_{f,r} = A_{f,r} T^{B_{f,r}} \exp\left(-\frac{C_{f,r}}{T}\right), \\ k_{b,r} = A_{b,r} T^{B_{b,r}} \exp\left(-\frac{C_{b,r}}{T}\right), \\ K_c = \frac{k_f}{k_b}, \end{cases} \quad (3)$$

where  $A_{f,r}$ ,  $B_{f,r}$ ,  $C_{f,r}$ ,  $A_{b,r}$ ,  $B_{b,r}$ , and  $C_{b,r}$  are constant terms of the reaction equation, respectively.  $K_c$  is the equilibrium constant of the chemical reaction.

In this paper, a five-component ( $N_2$ ,  $O_2$ ,  $NO$ ,  $N$ , and  $O$ ) chemical kinetic model is used. The effect of the third body on the chemical reaction is considered. The five-component reaction model and reaction rate are shown in Table 1, and the third-body catalytic efficiency is shown in Table 2 [18].

**2.2. Governing Equation of Thermoelasticity.** The governing equation of thermoelasticity describes the law obeyed by distribution of internal temperature and stress under aerodynamic loads. Energy in the structure includes heat energy and deformation energy. The heat energy is marked by temperature, and deformation energy is marked by stress and strain. The governing equation of thermoelasticity can be written as follows:

$$\rho_s c_p \frac{\partial T}{\partial t} - \frac{\partial}{\partial x_i} \left( \lambda_i \frac{\partial T}{\partial x_i} \right) - \sigma_{ij} \frac{\partial \epsilon_{ij}}{\partial t} = q, \quad (4)$$

where  $t$  is the time.  $T$  is the temperature.  $\rho_s$  is the material density.  $c_p$  is the specific heat capacity.  $\lambda_i$  is the thermal con-

TABLE 1: Gupta chemical reaction model and reaction rate constants.

Number	Reaction equation	$A_{f,r}$	$B_{f,r}$	$C_{f,r}$
1	$O_2 + M_1 \rightleftharpoons 2O + M_1$	1.00E19	-1.5	4.947E8
2	$N_2 + M_2 \rightleftharpoons 2N + M_2$	3.00E19	-1.6	9.412E8
3	$NO + M_3 \rightleftharpoons N + O + M_3$	1.10E14	0	6.227E8
4	$NO + O \rightleftharpoons N + O_2$	2.40E6	1	1.598E8
5	$N_2 + O \rightleftharpoons NO + N$	1.8E11	0	3.193E8

TABLE 2: Catalytic efficiency of the third body.

	$O_2$	$N_2$	$N$	$O$	$NO$
$M_1$	0.2	0.2	1	1	0.2
$M_2$	0.233	0.233	1	1	0.233
$M_3$	0.05	0.05	1	1	1

ductivity of material.  $\sigma_{ij}$  and  $\epsilon_{ij}$  are the stress tensor and strain tensor, respectively.  $q$  is the heat flux.

**2.3. Coupling Interface.** The coupling interface of the fluid-thermal-structural model needs to meet the deformation coordination and the energy conservation. The deformation of the structure is coordinated with the fluid boundary.

The energy conservation of the interface is shown in Equation (5). Figure 1 illustrates the energy conservation relation at the coupling interface.

$$q = q_{conv} + q_{rad-in} - q_{rad-out}, \quad (5)$$

where  $q_{conv}$  is the aerothermal heat flux.  $q_{rad-in}$  is the radiation heating heat flux by the flow field.  $q_{rad-out}$  is the radiative heat flux by the structure.

**2.4. Fluid-Thermal-Structural Coupling Strategy.** Multiphysics coupling issue is a complex process between aerothermodynamics in fluid and thermo-structural dynamics in solid through a fluid-solid coupling interface. According to the physical space, it can be divided into the fluid domain and solid domain. As shown in Figure 2,  $\Omega_f$  and  $\Omega_s$  represent the fluid domain and solid domain, respectively, and  $\Gamma$  represents the coupling interface. The spatial dispersion and time integration in the fluid domain are independent of those in the solid domain. As the computational grids of the two domains have different topological forms, data between two regions of mismatched grids is transferred by the mesh-based parallel code coupling interface (Mpcci). Mpcci is a standard computing program to couple multiphysical fields in distributed parameter models. The data association is carried out based on a neighborhood search. Straightforward interpolation is conducted utilizing shape function mapping for the interpolation of the heat flux, pressure, and temperature. Figure 3 shows the data transfer between mismatched grids.

According to the coupling characteristics, the fluid-thermal-structural coupling model is shown in Figure 4. It

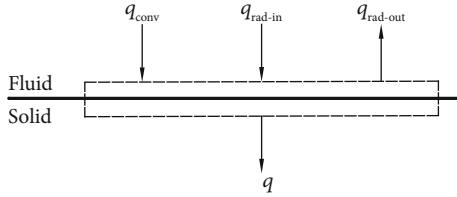


FIGURE 1: Energy conservation at the coupling interface.

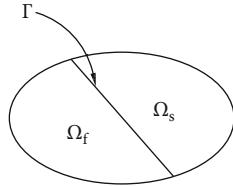


FIGURE 2: Fluid and solid domain.

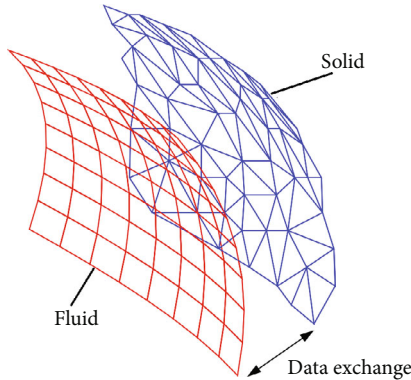


FIGURE 3: Data transfer of unmatched grids.

represents a two-way coupling relation between the aerothermodynamic environment of the flow field and the structural thermal response of the nose cap. The initial conditions and boundary conditions are defined in advance, which include the nose cap shape and the flow field conditions. The wall pressure and heat flux can be obtained by numerical calculation of the flow field. The response of the nose cap can be obtained by applying the pressure and heat flux to the nose cap structure. Heat flux, wall pressure, wall temperature, and wall position are transferred by Mpcci. This calculation process is repeated cyclically until the total calculation time is reached. The Abaqus ALE (arbitrary Lagrangian-Eulerian) mesh adaptive technology is used to remesh the internal grids of the model, thus avoiding the excessive deformity of the grids and finally realizing the simulation of the structural deformation of the nose cap.

The two-way loosely coupling strategy is shown in Figure 5 and can be summarized as follows:

- (1) At time  $t_0$ , the initial temperature and displacement of the structure are transferred to the fluid domain as the boundary conditions for the flow field

- (2) Based on the applied boundary conditions, the steady flow field is calculated in the fluid domain to obtain the wall heat flux and pressure
- (3) The wall heat flux and pressure of the flow field are transferred to the solid domain as boundary conditions for structure calculation
- (4) Based on the applied wall boundary conditions, the transient heat transfer and deformation are calculated in the solid domain, and the temperature and deformation distribution of the structure at time  $t_1$  are finally obtained
- (5) The temperature and position of the wall at time  $t_1$  are transferred to the fluid domain as the boundary condition of the flow field
- (6) At this point, the calculation of a coupling time step is completed, and then, the next coupling time step is continued and so on until the total coupling time is over

**2.5. Verification of the Numerical Model for Chemical Nonequilibrium Flow.** A cylinder model was considered for validating the numerical model for chemical nonequilibrium flow. Its experimental study was conducted in the pure air of DLR HEG [19]. The free stream velocity was 4776 m/s, the pressure was 687 Pa, the temperature was 694 K, and the wall temperature was 300 K. The initial mass fractions of  $N_2$ ,  $O_2$ ,  $N$ ,  $O$ , and  $NO$  were 0.23, 0.77, 0, 0, and 0, respectively. The diameter of the cylinder model was 90 mm, and the length was 380 mm. The computational grids and boundary conditions of the model are shown in Figure 6.

The calorimetric perfect gas model and five-component ( $N_2$ ,  $O_2$ ,  $NO$ ,  $O$ , and  $N$ ) chemical nonequilibrium gas model were established, respectively. Figure 7 is the distribution of the Mach number along a stationary line with different gas models. The detachment distance of shock wave using the calorimetric perfect gas model is 15.1 mm, and that using the chemical nonequilibrium model is 11.8 mm, which is more consistent with the experimental value of 11.9 mm. Figure 8 is the comparison contour between the numerical and experimental results. It can be seen that the numerical result using the chemical nonequilibrium gas model is in good agreement with the experimental result, which also verifies the reliability of the numerical chemical nonequilibrium model.

### 3. Fluid-Thermal-Structural Coupling Model of the Nose Cap

**3.1. Description of the Nose Cap.** The fluid-thermal-structural coupling is carried out with a typical nose cap. The geometry of the nose cap is shown in Figure 9, and its detailed dimensions can be found in Reference [5]. The basic idea of the nose cap is to couple C/SiC to  $ZrB_2/SiC$  in order to create a multimaterial structure to withstand the severe condition.  $ZrB_2/SiC$  is used in the tip of the nose cap to withstand extreme aerothermal load. C/SiC is used in the outer dome of the nose cap to reduce weight. Graphite is used in the inner

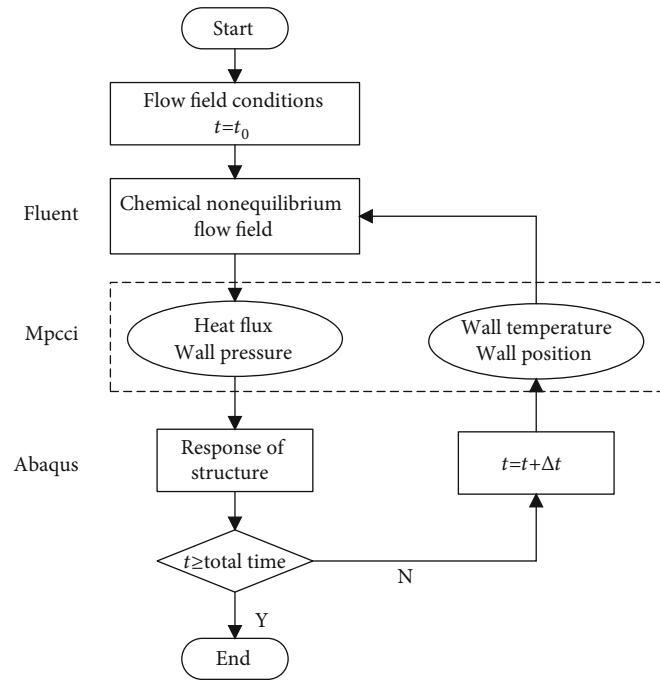


FIGURE 4: Fluid-thermal-structural coupling process.

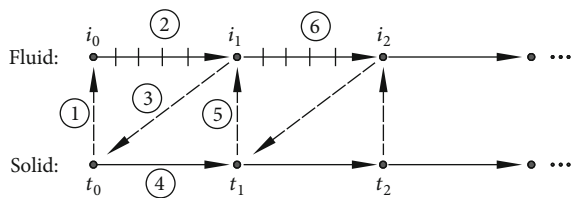


FIGURE 5: Two-way loosely coupling strategy.

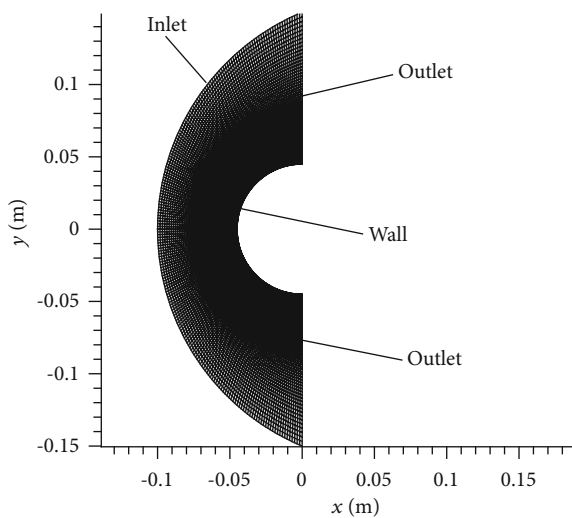


FIGURE 6: The computational grid.

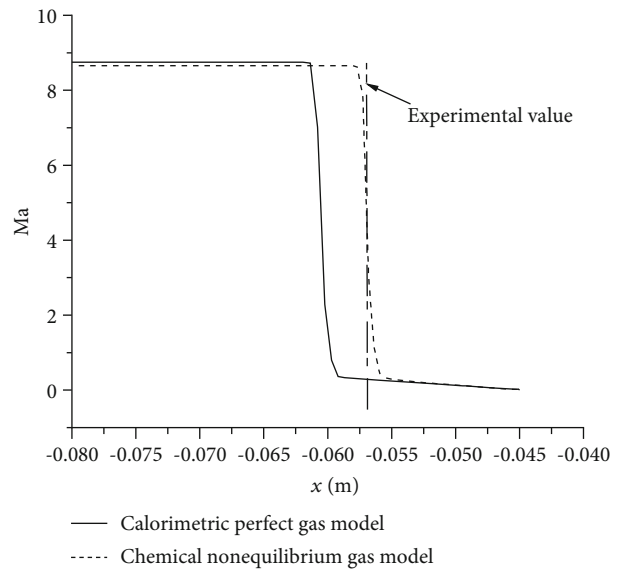
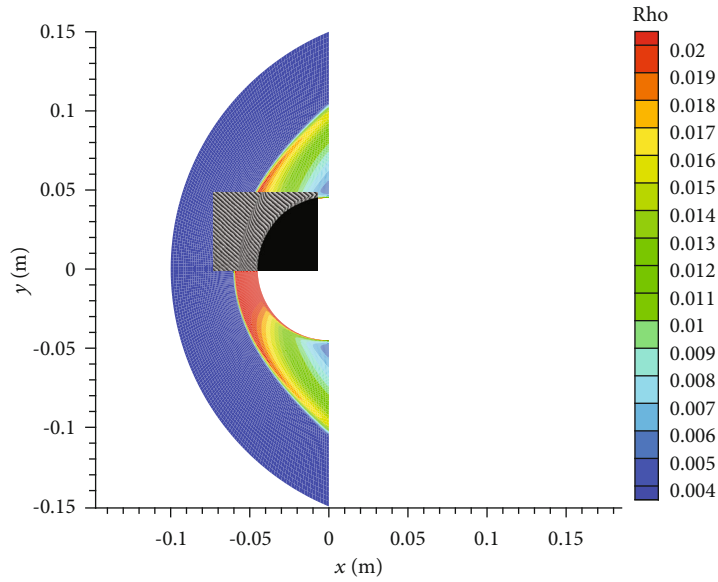


FIGURE 7: Distribution of the Mach number along a stationary line.

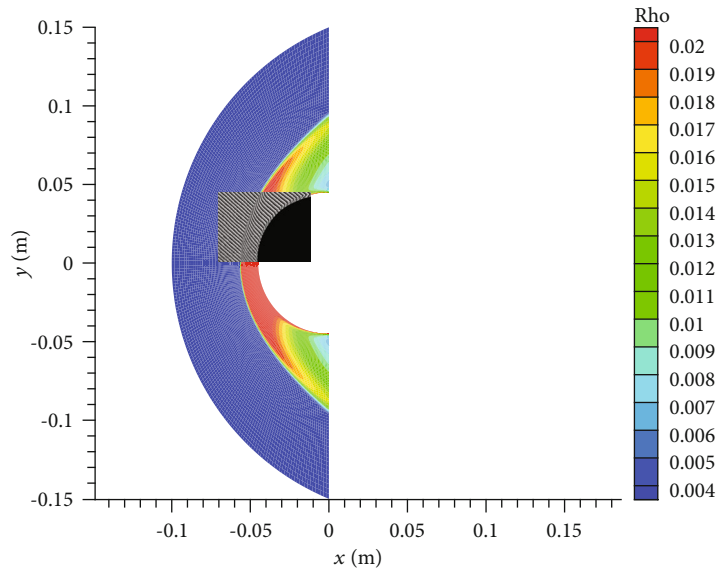
dome to increase thermal capacity. The parts of the nose cap are connected by the titanium alloy pin. The properties of materials are shown in Table 3.

The inflow conditions are shown in Table 4. The mass fractions of  $N_2$  and  $O_2$  are 77% and 23%, respectively.

**3.2. Fluid-Thermal-Structural Coupling Model.** The fluid-thermal-structural coupling analysis of the nose cap is carried out by using the two-way coupling strategy. The total coupling time is 200 s, and the coupling time step is 0.01 s. The



(a) Calorimetric perfect gas model



(b) Chemical nonequilibrium gas model

FIGURE 8: Comparison between the numerical and experimental results.

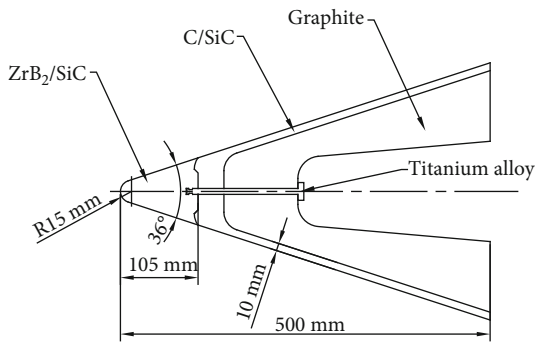


FIGURE 9: Geometry of the nose cap.

effect of chemical nonequilibrium is considered in the flow field. The wall is noncatalytic, and the effects of heat transfer and deformation are considered in the structure. Fluent is used to simulate the flow field. The CFD computational grids are shown in Figure 10(a), and the grids have 20592 elements, which are refined near the wall. Abaqus is used to simulate the response of the nose cap. As shown in Figure 10(b), the number of FEA grid elements is 9346. Mpcci is used to transfer the data of the fluid-solid interface. Because of the symmetry, only one-half of the nose cap is modeled.

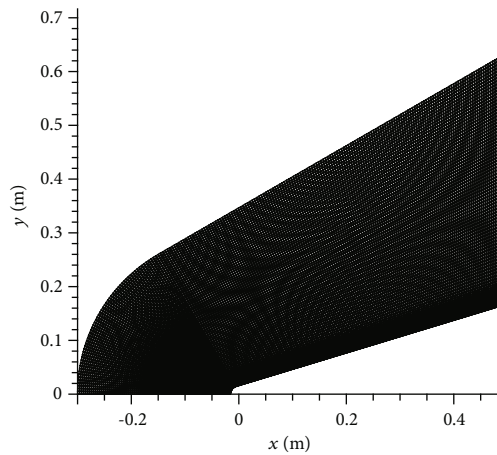
The boundary conditions of the nose cap model are as follows: symmetrical boundary conditions applied to the symmetrical axis, fixed constraints at the bottom, and initial temperature of the nose cap (300 K). The effect of material ablation is not considered in the model.

TABLE 3: Material properties of the nose cap.

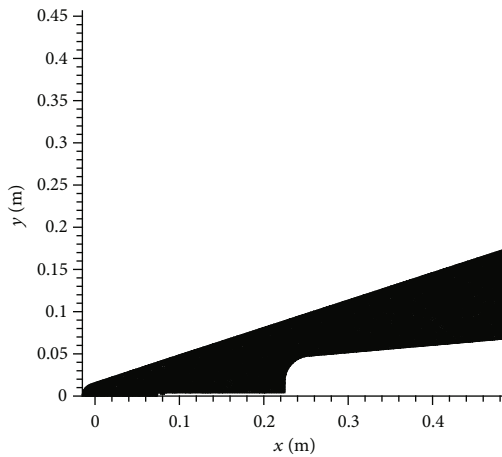
	ZrB <sub>2</sub> /SiC	C/SiC	Titanium alloy	Graphite
Density (kg/m <sup>3</sup> )	6060	1870	4430	1730
Specific heat (J/kg·K)	520 (300 K)	682 (300 K)	526	720
	850 (2200 K)	1602 (2200 K)		
Heat conductivity coefficient (W/m·K)	79.87 (300 K)	11.74 (273 K)	6.7	90
	85 (1473 K)	17.2 (1673 K)		
Young's modulus (Gpa)	506	45	114	10.4
Tensile strength (Mpa)	491	200	965	30
Poisson ratio	0.13	0.3	0.33	0.3
Thermal expansion coefficient	3E-6	2.25E-6	10.8E-6	2E-6
Emissivity	0.55	0.83	0.5	0.75

TABLE 4: Free inflow conditions.

Ma	Altitude (km)	Temperature (K)	Pressure (Pa)
6	20	217	5475
7.5	20	217	5475
9	20	217	5475

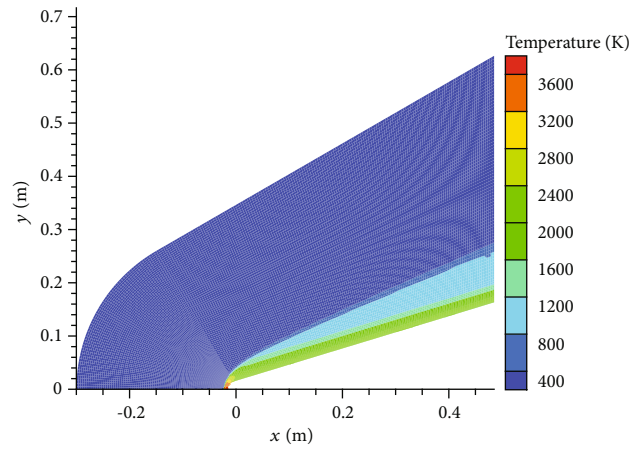


(a) CFD grids of the flow field

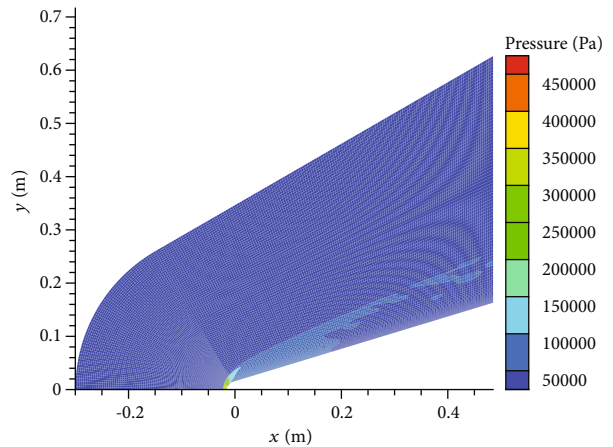


(b) FEM grids of the nose cap

FIGURE 10: Grids of the computational domain.



(a) Temperature contour of the flow field



(b) Static pressure contour of the flow field

FIGURE 11: Flow features at 100 s.

## 4. Results and Discussion

4.1. *Response of the Nose Cap.* The inflow Mach number is 7.5. Figure 11 shows the temperature and pressure contours of the flow field at 100 s. The flow field can be divided into the far-field free inflow zone and bow shock zone. The

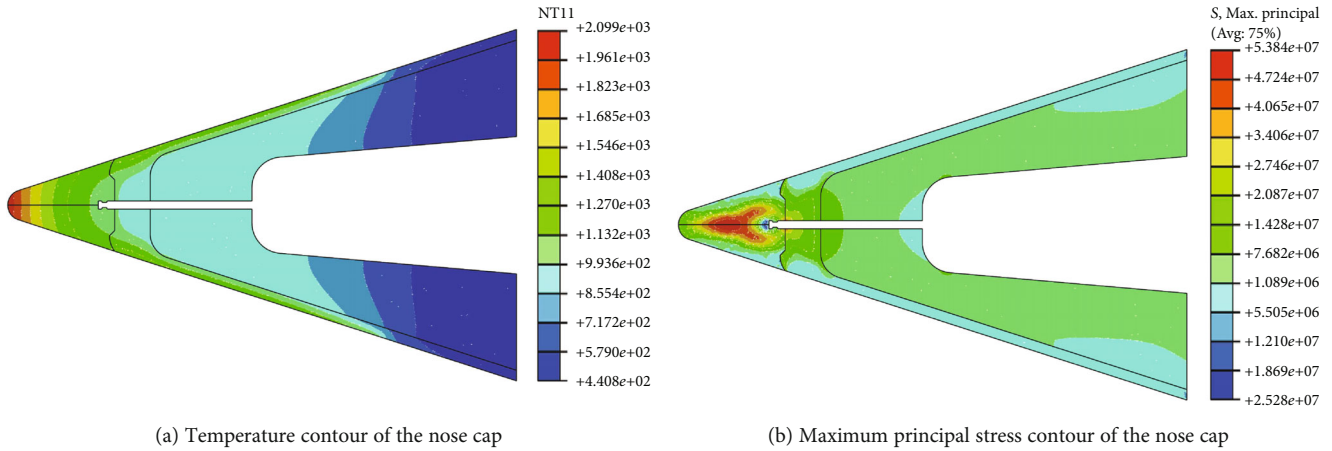


FIGURE 12: Nose cap features at 100 s.

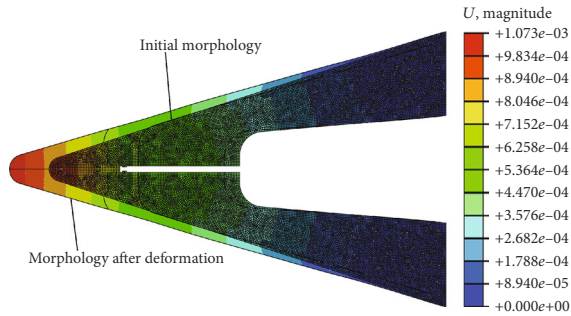


FIGURE 13: Deformation contour of the nose cap at 100 s.

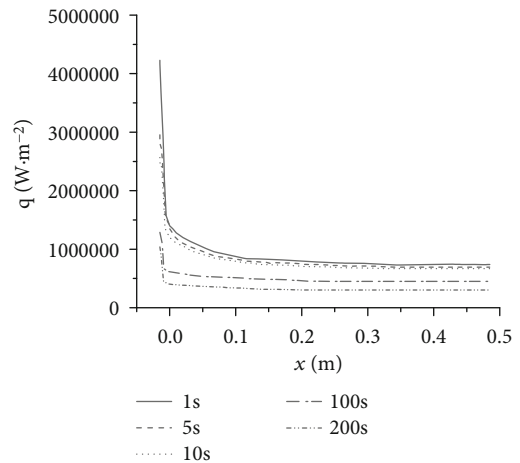


FIGURE 14: Heat flux along the nose cap wall.

highest temperature of the flow field is 3680 K, which brings severe challenges to the nose cap structure.

The response of the nose cap under aerothermodynamic loads is analyzed. Figure 12 shows the temperature and the maximum principal stress contours of the nose cap at 100 s. The highest temperature occurs in the nose cap head area. As the ceramic material is brittle, its fracture failure is reflected by the maximum principal stress. The peak of maximum principal stress occurs in the region of the head.

Figure 13 is the deformation contour of the nose cap at 100 s. It can be seen that under the aerodynamic load and the thermal expansion, the nose cap has certain deformation. The largest deformation occurs at the tip of the nose cap, and the largest deformation value is 1.07 mm.

**4.2. Effect of Flight Time on Nose Cap Response.** Figure 14 is the evolution of heat flux along the nose cap wall. The maximum heat flux is in the stagnation region and decreases accordingly away from the stagnation area. As time goes on, the heat flux in the stagnation area decreases rapidly. This is because the heat flux is related to the temperature gradient near the wall. The larger the temperature gradient is, the larger the heat flux is. At the initial time, the wall temperature of the nose cap is lower and the temperature gradient near the wall is larger, which leads to a larger heat flux. With the heat transferring to the material, the temperature of the nose cap increases gradually, which makes the temperature

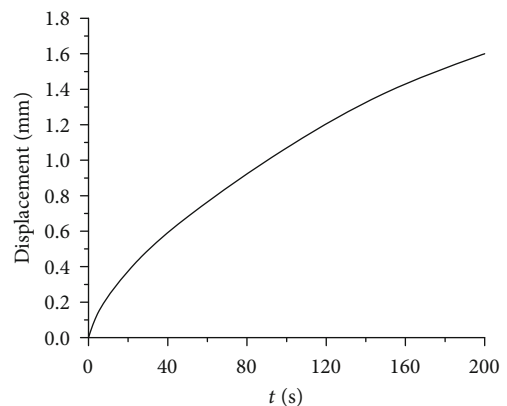


FIGURE 15: Evolution of nose cap tip deformation with time.

gradient and the heat flux decrease. The result shows that if the uncoupled model is used, the change of heat flux cannot be predicted and the thermal load will be overestimated.

Figure 15 is the evolution of nose cap tip displacement with time. It can be seen that the displacement of

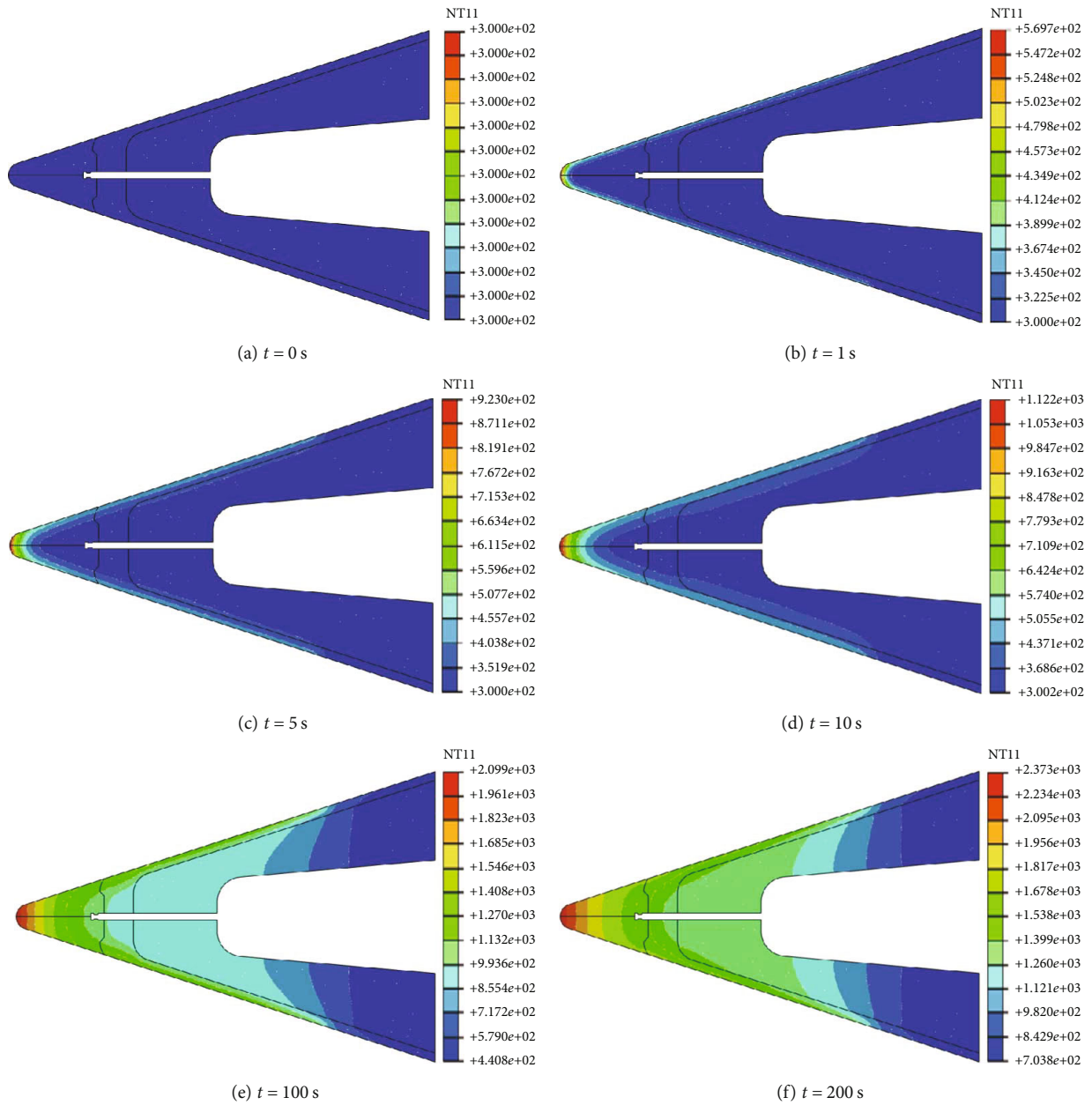


FIGURE 16: Evolution of temperature distribution of the nose cap.

the nose cap tip increases gradually with time, which will affect the prediction of aerodynamic force and aerodynamic heat.

Figure 16 shows the temperature distribution of the nose cap at different times. As the effect of aerothermal load, the heat accumulates rapidly near the stagnation region, which leads to the rapid increase in the structure temperature. As time goes on, the heat accumulates continuously and the temperature of the structure is also constantly rising. At the same time, the heat is gradually transferred to the deep region of the structure.

Figure 17 shows the maximum principal stress distribution at different times. As temperature gradient at the tip is largest, the peak of maximum principal stress appears

at the top of the nose cap. As time goes on, the heat begins to transmit to the deep region, the temperature gradient decreases, and the peak value of the maximum principal stress decreases. The position of the peak of maximum principal stress gradually moves to the deep region of the nose cap. If the structure design and material selection are unreasonable, it will cause thermal and mechanical damage to the structure.

Figures 18 and 19 are the distributions of temperature and maximum principal stress along the axis of the nose cap at different times. The highest temperature position is at the tip of the nose cap, and temperature increases gradually with the advance of flight time. The peak value of the maximum principal stress begins to appear at the front of

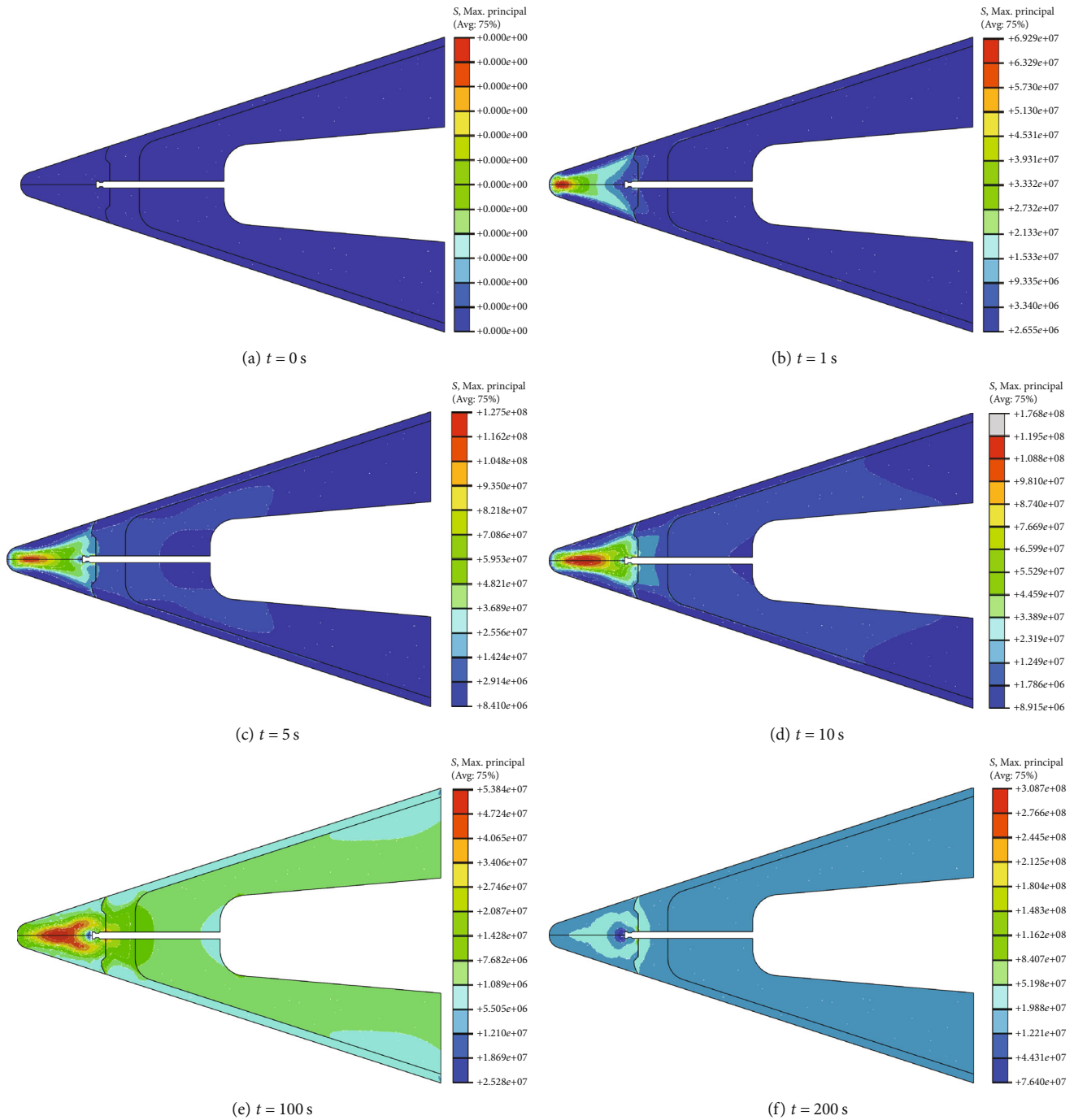


FIGURE 17: Evolution of maximum principal stress distribution of the nose cap.

the nose cap. As time goes on, the peak of maximum principal stress gradually decreases after reaching a certain value and the position gradually moves towards the inside of the nose cap and finally tends to be stable.

**4.3. Effect of the Mach Number on Nose Cap Response.** The influence of the Mach number on nose cap response is analyzed.  $Ma = 6$ ,  $Ma = 7.5$ , and  $Ma = 9$  are used to simulate the response of the nose cap, while other parameters are unchanged. Figures 20 and 21 show the highest temperature

and the peak of maximum principal stress distributions with different Mach numbers. The maximum temperature and the peak of maximum principal stress increase gradually with the increase in the Mach number. The peak of maximum principal stress increases rapidly at the initial stage and reaches its peak value at around 6 s. This is mainly because, at the beginning, heat flux gathers at the tip, forming a larger temperature gradient. As time goes on, the peak value of maximum principal stress gradually decreases and finally approaches a smaller value.

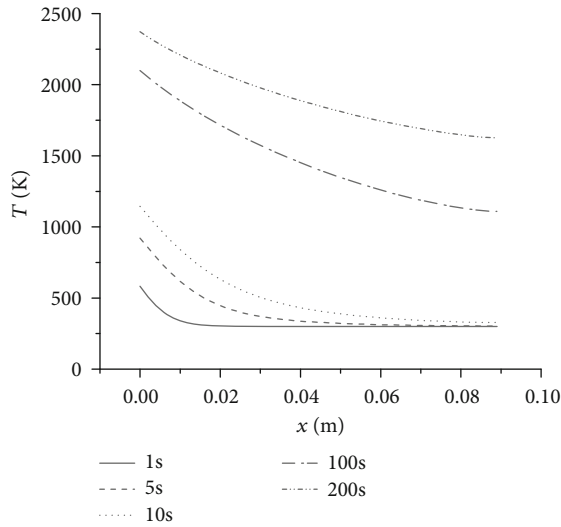


FIGURE 18: Temperature distribution along the axis.

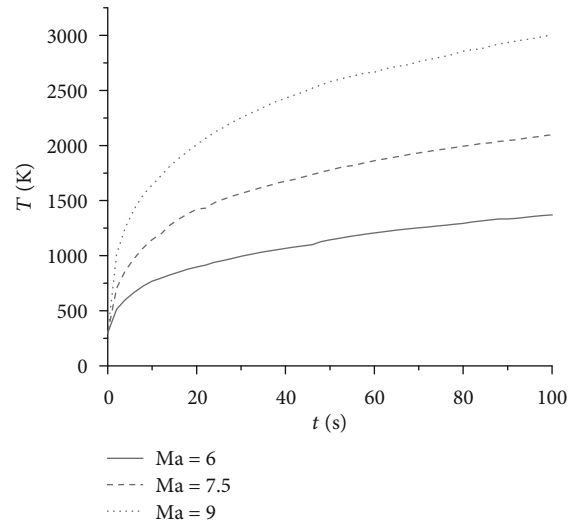


FIGURE 20: Effect of the Mach number on the highest temperature.

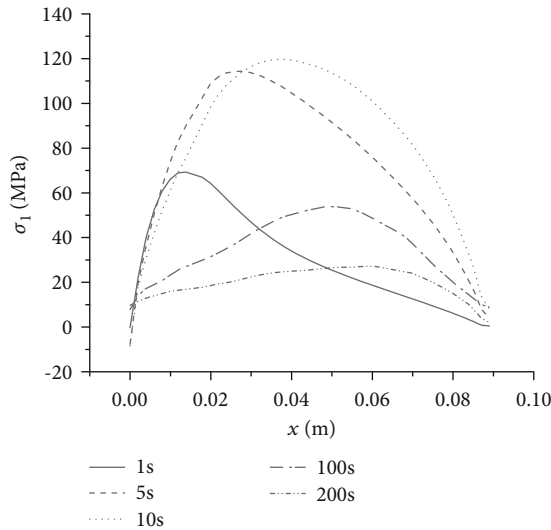


FIGURE 19: Maximum principal stress distribution along the axis.

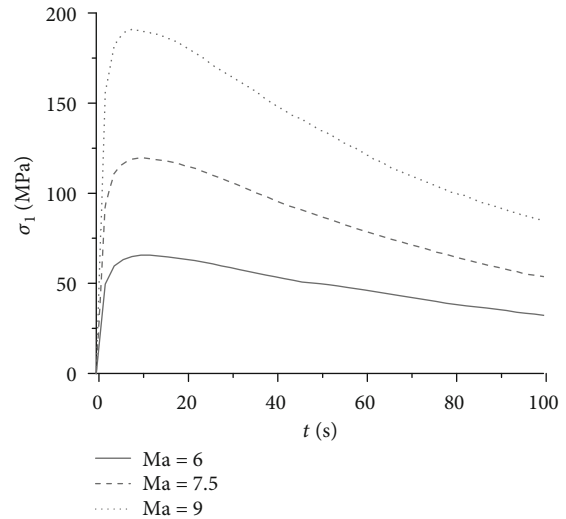


FIGURE 21: Effect of the Mach number on the peak of maximum principal stress.

## 5. Conclusions

In the present paper, a fluid-thermal-structural model was established to study the response of the nose cap in a hypersonic environment. The main conclusions are listed as follows:

- (1) There is a close coupling relation between the hypersonic environment and response of the nose cap. The fluid-thermal-structural model can effectively predict the response of the nose cap under a hypersonic environment
- (2) At the initial stage, the highest temperature and the peak value of maximum principal stress appear at the nose cap head. As time goes on, the highest temperature gradually increases and finally tends to be stable. When the peak of maximum principal stress

reaches a certain value, it gradually decreases and the position of the peak of maximum principal stress gradually moves to the inside of the nose cap and eventually tends to be stable

- (3) With the increase in the Mach number, the highest temperature and the peak of maximum principal stress of the nose cap structure increase

Based on the investigation of the thermo-structural response of the structure, multiobjective optimization for the nose cap will be conducted in the future.

## Data Availability

All data included in this study are available upon request by contacting the corresponding author.

## Conflicts of Interest

The authors declare that they have no conflicts of interest.

## Acknowledgments

This work was supported by National Key Scientific Instrument and Equipment Development Projects of China (No. 2011YQ140145) and Hebei Science and Technology Department Research Fund (No. 17211117).

## References

- [1] D. Sziroczak and H. Smith, "A review of design issues specific to hypersonic flight vehicles," *Progress in Aerospace Sciences*, vol. 84, pp. 1–28, 2016.
- [2] A. Cecere, R. Savino, C. Allouis, and F. Monteverde, "Heat transfer in ultra-high temperature advanced ceramics under high enthalpy arc-jet conditions," *International Journal of Heat and Mass Transfer*, vol. 91, pp. 747–755, 2015.
- [3] Y. Zhu, W. Peng, R. Xu, and P. Jiang, "Review on active thermal protection and its heat transfer for airbreathing hypersonic vehicles," *Chinese Journal of Aeronautics*, vol. 31, no. 10, pp. 1929–1953, 2018.
- [4] R. J. Tobe and R. V. Grandhi, "Hypersonic vehicle thermal protection system model optimization and validation with vibration tests," *Aerospace Science and Technology*, vol. 28, no. 1, pp. 208–213, 2013.
- [5] R. Borrelli, A. Riccio, D. Tescione, R. Gardi, and G. Marino, "Thermo-structural behaviour of an UHTC made nose cap of a reentry vehicle," *Acta Astronautica*, vol. 65, no. 3-4, pp. 442–456, 2009.
- [6] R. Borrelli, A. Riccio, D. Tescione, R. Gardi, and G. Marino, "Numerical/experimental correlation of a plasma wind tunnel test on a UHTC-made nose cap of a reentry vehicle," *Journal of Aerospace Engineering*, vol. 23, no. 4, pp. 309–316, 2010.
- [7] M. G. Persova, Y. G. Soloveichik, V. K. Belov et al., "Modeling of aerodynamic heat flux and thermoelastic behavior of nose caps of hypersonic vehicles," *Acta Astronautica*, vol. 136, pp. 312–331, 2017.
- [8] A. Tabiei and S. Sockalingam, "Multiphysics coupled fluid/thermal/structural simulation for hypersonic reentry vehicles," *Journal of Aerospace Engineering*, vol. 25, no. 2, pp. 273–281, 2012.
- [9] F. Chen, H. Liu, and S. Zhang, "Coupled heat transfer and thermo-mechanical behavior of hypersonic cylindrical leading edges," *International Journal of Heat and Mass Transfer*, vol. 122, pp. 846–862, 2018.
- [10] F. Chen, H. Liu, and S. Zhang, "Time-adaptive loosely coupled analysis on fluid–thermal–structural behaviors of hypersonic wing structures under sustained aeroheating," *Aerospace Science and Technology*, vol. 78, pp. 620–636, 2018.
- [11] D. J. Munk, D. Verstraete, and G. A. Vio, "Effect of fluid–thermal–structural interactions on the topology optimization of a hypersonic transport aircraft wing," *Journal of Fluids and Structures*, vol. 75, pp. 45–76, 2017.
- [12] A. J. Culler and J. J. McNamara, "Impact of fluid–thermal–structural coupling on response prediction of hypersonic skin panels," *AIAA Journal*, vol. 49, no. 11, pp. 2393–2406, 2011.
- [13] B. A. Miller and J. J. McNamara, "Efficient fluid–thermal–structural time marching with computational fluid dynamics," *AIAA Journal*, vol. 56, no. 9, pp. 3610–3621, 2018.
- [14] K. Bhide, K. Siddappaji, and S. Abdallah, "Influence of fluid–thermal–structural interaction on boundary layer flow in rectangular supersonic nozzles," *Aerospace*, vol. 5, no. 2, pp. 33–46, 2018.
- [15] S. Guo, J. Xu, Q. Qin, and R. Gu, "Fluid–thermal interaction investigation of spiked blunt bodies at hypersonic flight condition," *Journal of Spacecraft and Rockets*, vol. 53, no. 4, pp. 629–643, 2016.
- [16] A. R. Crowell, B. A. Miller, and J. J. McNamara, "Robust and efficient treatment of temperature feedback in fluid–thermal–structural analysis," *AIAA Journal*, vol. 52, no. 11, pp. 2395–2413, 2014.
- [17] B. A. Miller and J. J. McNamara, "Time-marching considerations for response prediction of structures in hypersonic flows," *AIAA Journal*, vol. 53, no. 10, pp. 3028–3038, 2015.
- [18] R. N. Gupta, J. M. Yos, R. A. Thompson, and K.-P. Lee, "A review of reaction rates and thermodynamic and transport properties for an 11-species air model for chemical and thermal nonequilibrium calculations to 30000 K," NASA STI/Recon Technical Report, 1990.
- [19] J. M. Schramm, K. Hannemann, W. Beck, and S. Karl, "Cylinder shock layer density profiles measured in high enthalpy flows in HEG," in *22nd AIAA Aerodynamic Measurement Technology and Ground Testing Conference*, pp. 1–9, Saint Louis, MO, USA, 2002.